SUPPLEMENTARY FIGURES

ImmunoPET of Ovarian and Pancreatic Cancer with AR9.6, a Novel MUC16-Targeted Therapeutic Antibody

Sai Kiran Sharma[1], Kyeara N. Mack[1,2,3], Alessandra Piersigilli[4], Jacob Pourat[1], Kimberly J. Edwards[1], Outi Keinänen[1,5], Maria S. Jiao[4], Huiyong Zhao[6], Brandy White[7], Cory L. Brooks[7], Elisa de Stanchina[6], Madi R. Madiyalakan[8], Michael A. Hollingsworth[9], Prakash Radhakrishnan[9], Jason S. Lewis[1,3,10,11] and Brian M. Zeglis[1,5,10,12,13*]*

[1] Department of Radiology, Memorial Sloan Kettering Cancer Center, New York, NY, USA

[2] Department of Pharmacology, Weill Cornell Medical College, New York, NY, USA

[3] Molecular Pharmacology Program, Memorial Sloan Kettering Cancer Center, New York, NY, USA

[4] Tri-Institutional Laboratory of Comparative Pathology, Memorial Sloan Kettering Cancer Center, Weill Cornell Medical College, and The Rockefeller University, NY, USA

[5] Department of Chemistry, Hunter College, City University of New York, New York, NY, 10065

[6] Anti-Tumor Assessment Core, Memorial Sloan Kettering Cancer Center, NY, USA

[7] Department of Chemistry, California State University, Fresno, CA, USA

[8] Quest PharmaTech Inc., Edmonton, AB, Canada

[9] Eppley Institute for Research in Cancer and Allied Diseases, Fred and Pamela Buffett Cancer Center, University of Nebraska Medical Center, Omaha, NE, USA

[10] Department of Radiology, Weill Cornell Medical College, New York, NY, USA

[11] Radiochemistry and Molecular Imaging Probes Core, Memorial Sloan Kettering Cancer Center, New York, NY, USA

[12] Ph.D. Program in Chemistry, The Graduate Center of the City University of New York, New York, NY, 10016, United States

[13] Ph.D. Program in Biochemistry, The Graduate Center of the City University of New York, New York, NY, 10016, United States

SUPPLEMENTARY FIGURES

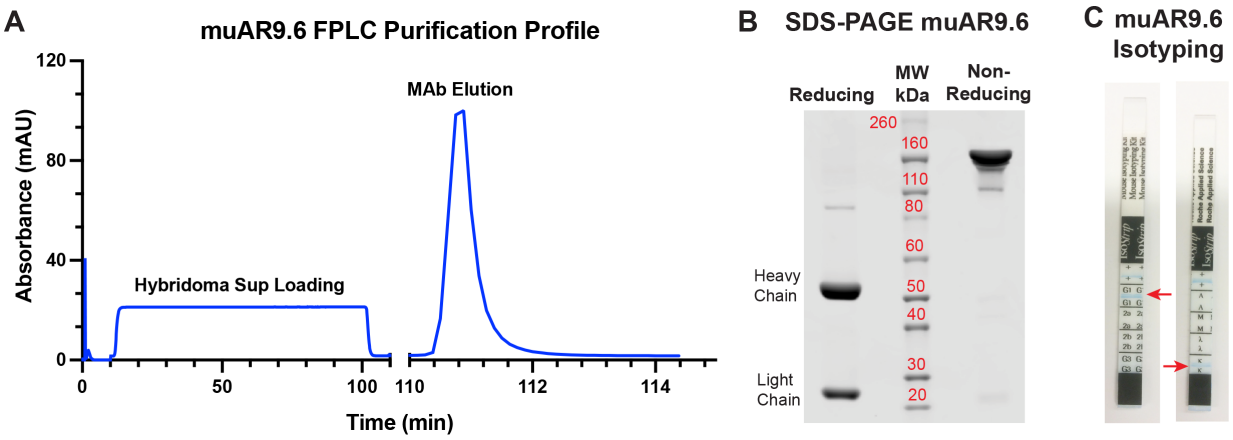

Figure S1. FPLC purification of hybridoma-expressed muAR9.6 antibody. (**A**) FPLC chromatogram showing protein G affinity chromatography-based single-step purification of murine mAb muAR9.6; (**B**) SDS-PAGE analysis of the purified muAR9.6 under reducing and non-reducing conditions; (**C**) Isotyping the purified muAR9.6 antibody revealed it to be a mouse IgG1 with a kappa light chain.

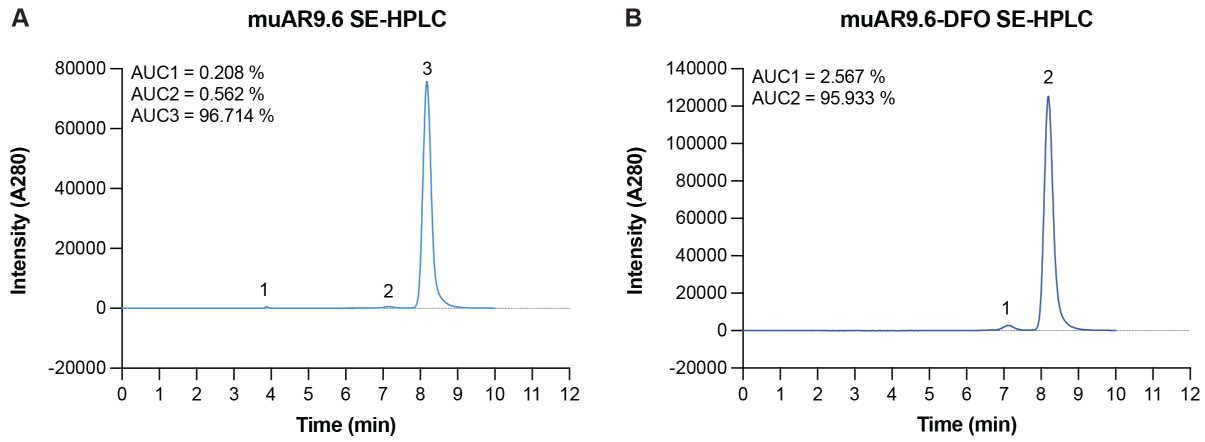

Figure S2. Size exclusion-high performance liquid chromatography (SE-HPLC) profiles of (A) muAR9.6 and (B) muAR9.6-DFO. SE-HPLC revealed ≥95% monomeric content (peak 3 in A) of muAR9.6 and its DFO-modified conjugate (peak 2 in B).

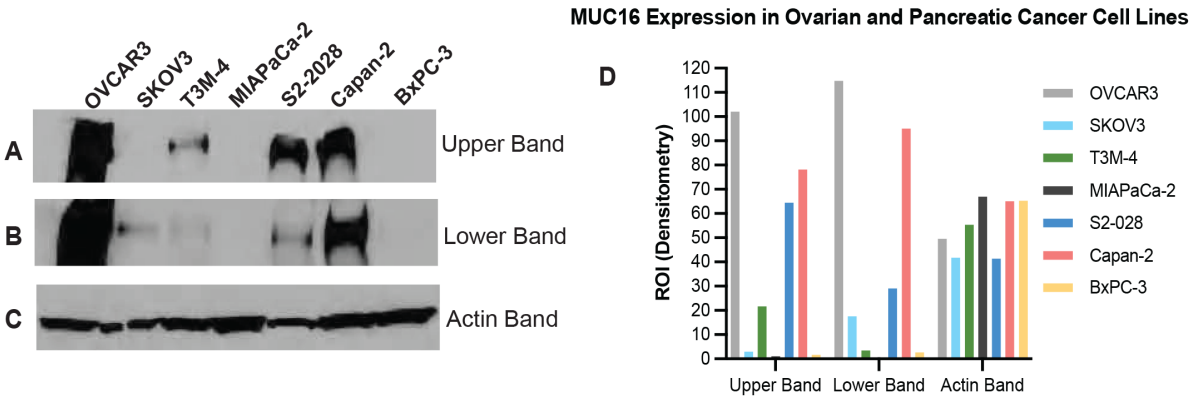

Figure S3. Comparative analysis of MUC16 expression in ovarian cancer (OVCAR3, SKOV3) and pancreatic cancer (T3M-4, MIAPaCa-2, S2-2028, Capan-2, BxPC-3) cell lines. Western blotting of cell lysates from the various ovarian and pancreatic cell lines revealed differential expression of two MUC16 epitopes: a higher molecular weight band (**A**) and a lower molecular weight band (**B**). (**C**) represents the actin band serving as a loading control; (**D**) Graph showing densitometric quantitation of the western blot by drawing ROIs on the respective bands.

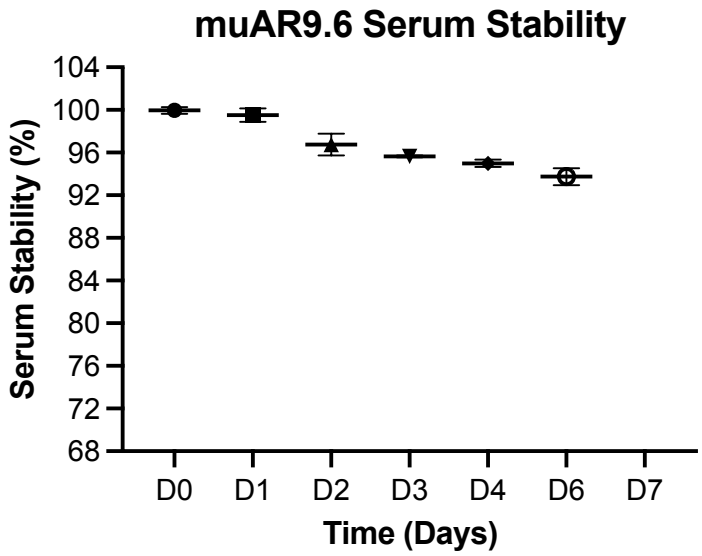

Figure S4. ***In vitro*** **serum stability of [^{89}Zr]Zr-DFO-muAR9.6.** [^{89}Zr]Zr-DFO-muAR9.6 demonstrated less than 7% demetallation via radio-iTLC after incubation in human AB type serum for 7 days at 37 °C.

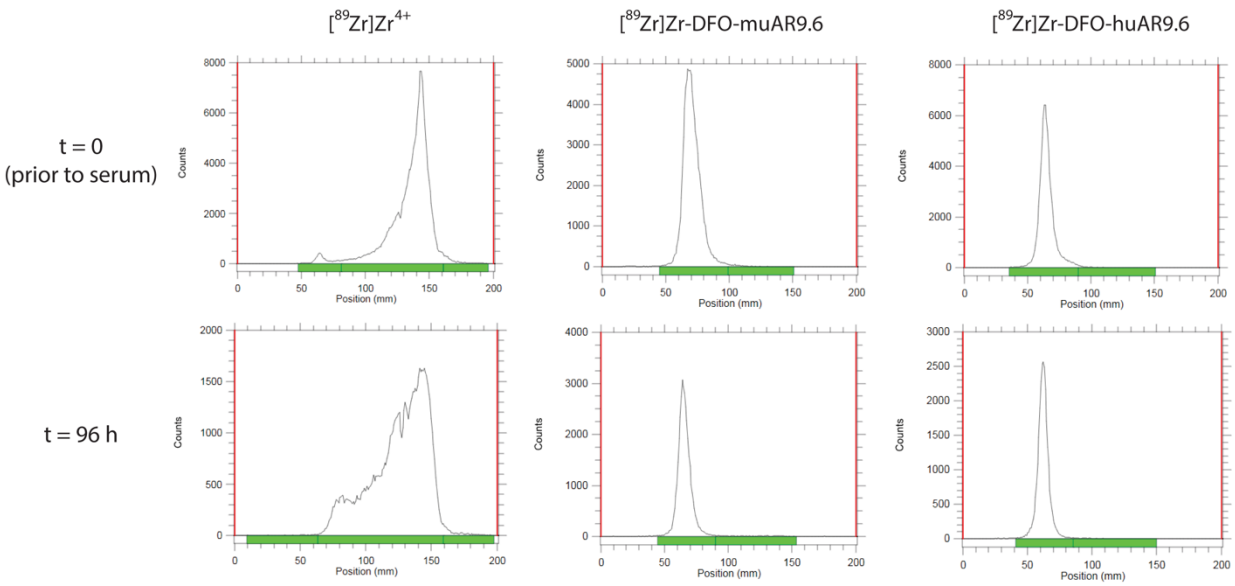

Figure S5. Radio-instant thin layer chromatography. Representative radio-iTLC chromatograms of free [^{89}Zr]Zr^{4+}, [^{89}Zr]Zr-DFO-muAR9.6, and [^{89}Zr]Zr-DFO-huAR9.6 prior to incubation in human AB type serum (top) and after 96 h of incubation in human AB type serum at 37 °C (bottom). Free [^{89}Zr]Zr^{4+} is clearly resolved from both ^{89}Zr-labeled radioimmunoconjugates.

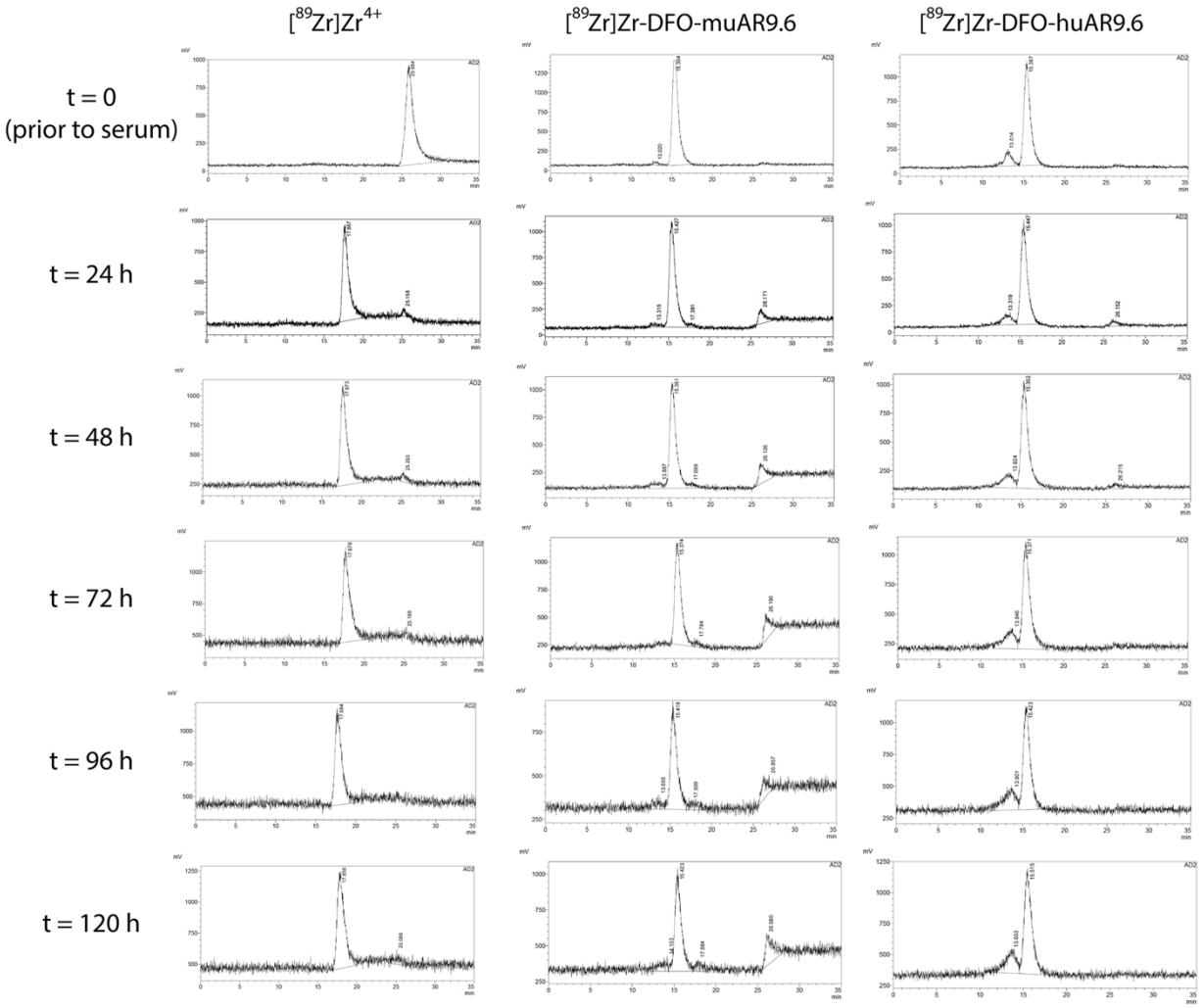

Figure S6. Radio-size exclusion HPLC. Radio-SE-HPLC chromatograms of free [^{89}Zr]Zr^{4+}, [^{89}Zr]Zr-DFO-muAR9.6, and [^{89}Zr]Zr-DFO-huAR9.6 prior to incubation in human AB type serum and after 24, 48, 72, 96, and 120 h of incubation in human AB type serum at 37 °C. Free [^{89}Zr]Zr^{4+} (t_R ~ 26 min), ^{89}Zr-labeled serum proteins (t_R ~ 17.5 min), and ^{89}Zr-labeled radioimmunoconjugates (t_R ~ 15.5 min) can be clearly resolved. [^{89}Zr]Zr-DFO-muAR9.6 shows no evidence of aggregation but does show some evidence of demetallation; however, neither the radio-iTLC data and *in vivo* data corroborate this behavior, suggesting it may be an artifact of this analytical method. [^{89}Zr]Zr-DFO-huAR9.6 shows no evidence of demetallation but does display evidence of some aggregation over the incubation period.

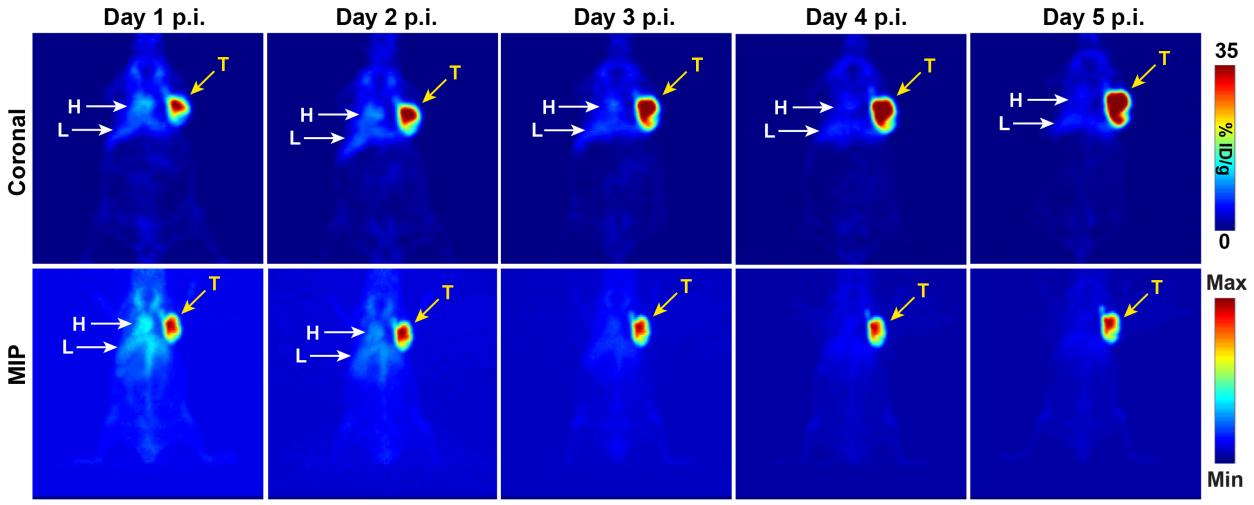

Figure S7. Longitudinal [^{89}Zr]Zr-DFO-muAR9.6 PET imaging of mice bearing subcutaneous OVCAR3 xenografts. Serial PET images of a nude mouse bearing a subcutaneous OVCAR3 tumor on the right shoulder. Mice were injected with 1.2 ± 0.1 mg/kg [^{89}Zr]Zr-DFO-muAR9.6 (255 ± 49.5 µCi; 9.4 ± 1.8 MBq; 29.6 ± 2.0 µg), and PET images were acquired every 24 h up to 5 d post-injection (p.i.). A gradual accretion of radioactivity in the tumor (T) can be seen with a concomitant decrease of radioactivity concentration in the blood [indicated by the heart (H)]. The maximum intensity projections have been scaled from 0-100%.

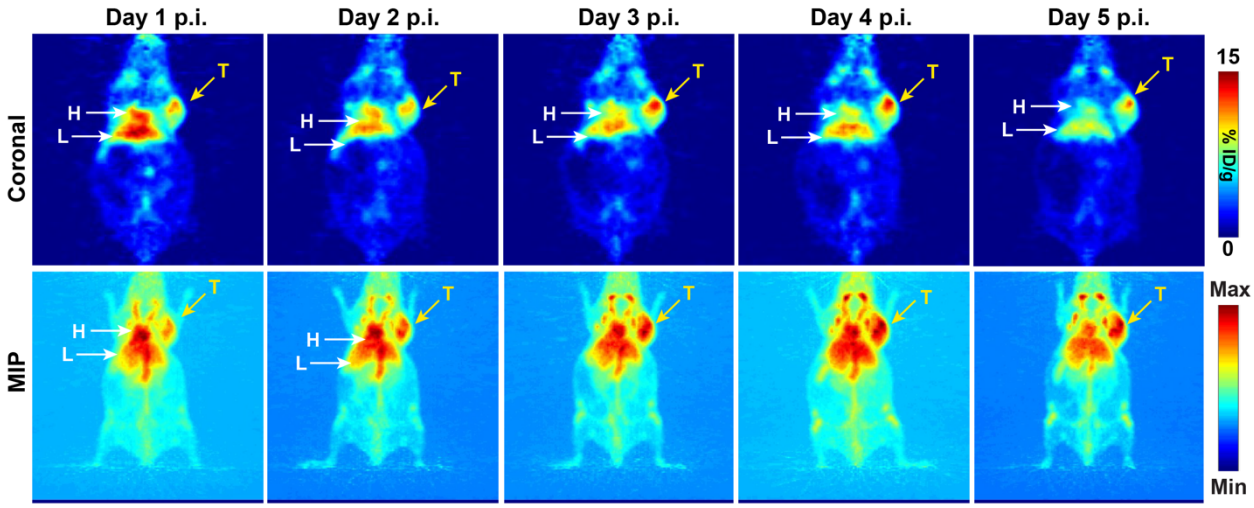

Figure S8. Longitudinal [^{89}Zr]Zr-DFO-muAR9.6 PET imaging of mice with subcutaneous SKOV3 xenografts. Serial PET images of a nude mouse bearing a subcutaneous SKOV3 tumor on the right shoulder. Mice were injected with 1.2 ± 0.1 mg/kg [^{89}Zr]Zr-DFO-muAR9.6 (255 ± 49.5 µCi; 9.4 ± 1.8 MBq; 29.6 ± 2.0 µg), and PET images were acquired every 24 h up to 5 d post-injection (p.i.). A gradual accretion of radioactivity in the tumor (T) can be seen; however, the vast majority of radioactivity remained in the blood, as indicated by the heart (H), the carotid arteries in the neck, and well perfused organs such as the liver (L). The maximum intensity projections have been scaled from 0-100%.

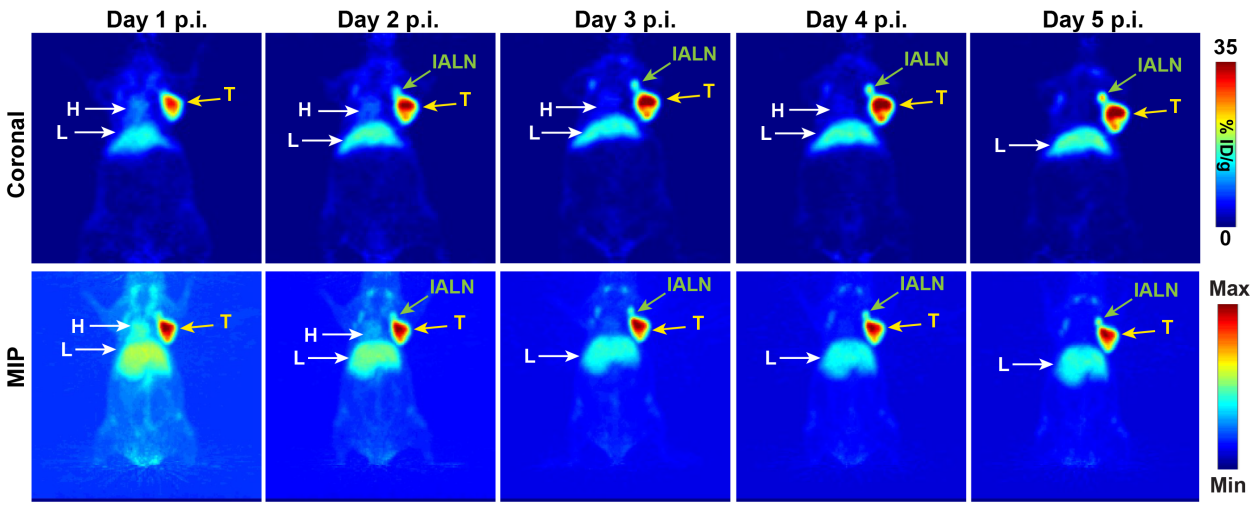

Figure S9. OVCAR3 tumor-bearing mice with uptake of [^{89}Zr]Zr-DFO-muAR9.6 in the lymph nodes also display high radioactivity concentrations in the liver. Serial PET images of a nude mouse bearing a subcutaneous OVCAR3 tumor on the right shoulder. Mice were injected with 1.2 ± 0.1 mg/kg [^{89}Zr]Zr-DFO-muAR9.6 (255 ± 49.5 µCi; 9.4 ± 1.8 MBq; 29.6 ± 2.0 µg), and PET images were acquired every 24 h up to 5 d post-injection (p.i.). A gradual accretion of the radioactivity in the tumor (T) can be seen with a concomitant decrease of radioactivity concentration in the blood – indicated by the heart (H). Notably, OVCAR3 tumor-bearing mice that showed accretion of radioactivity in the ipsilateral lymph node chain also showed higher than normal radioactivity concentrations in the liver (L) as early as 1 d p.i. The maximum intensity projections have been scaled from 0-100%.

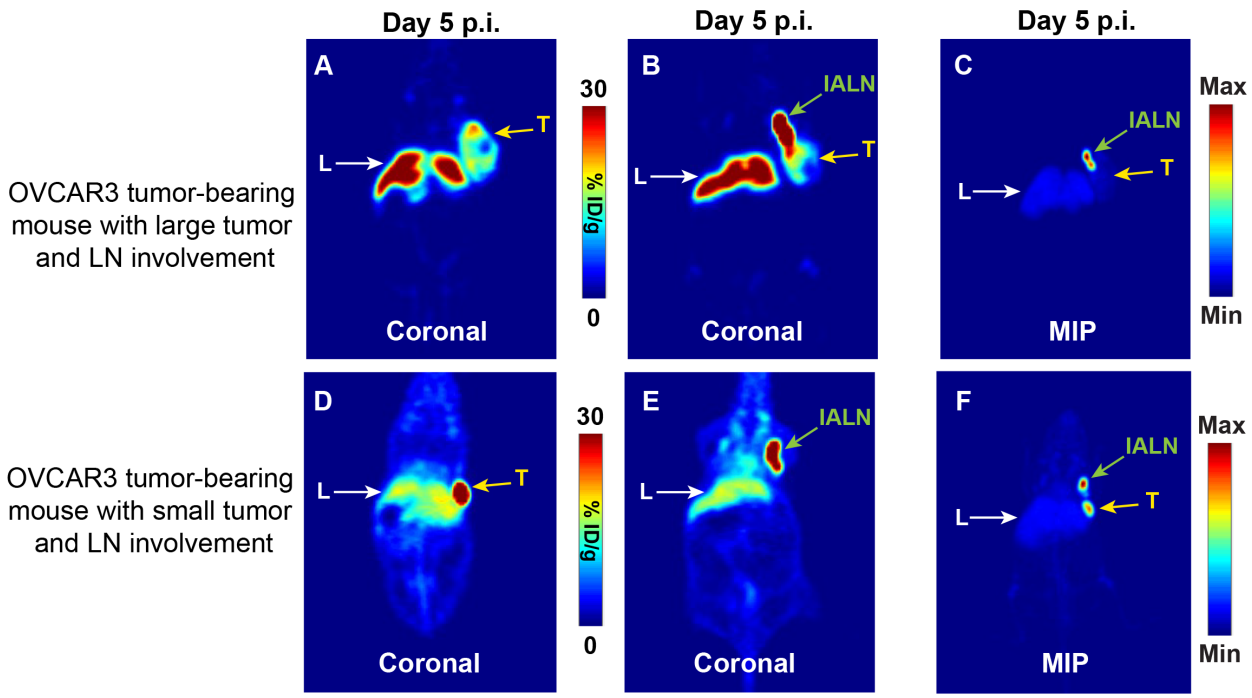

Figure S10. OVCAR3 tumor-bearing mice with high levels of uptake of [^{89}Zr]Zr-DFO-muAR9.6 in the lymph nodes also display high activity concentrations in the liver. (**A-C**) PET images acquired 5 d after the administration of [^{89}Zr]Zr-DFO-muAR9.6 in a mouse bearing a large subcutaneous OVCAR3 xenograft; (**A**) Coronal slice highlighting the relatively low uptake of activity in the tumor but high radioactivity concentration in the liver (L); (**B**) Coronal slice highlighting the high radioactivity concentration in the ipsilateral axillary lymph node (IALN) as well as the liver (L); (**C**) Maximum intensity projection (MIP) PET image of the same animal highlighting the relative radioactivity concentrations in the IALN, liver (L), and tumor (T); (**D-F**) PET images acquired 5 d after the administration of [^{89}Zr]Zr-DFO-muAR9.6 in a mouse bearing a small subcutaneous OVCAR3 xenograft; (**D**) Coronal slice highlighting the high uptake of activity in the tumor as well as the lower radioactivity concentration in the background liver (L); (**E**) Coronal slice highlighting the high radioactivity concentration in the ipsilateral axillary lymph node (IALN) as well as the liver (L); (**F**) Maximum intensity projection (MIP) PET image of the same animal highlighting the relative radioactivity concentrations in the IALN, tumor (T), and liver (L). The maximum intensity projections have been scaled from 0-100%.

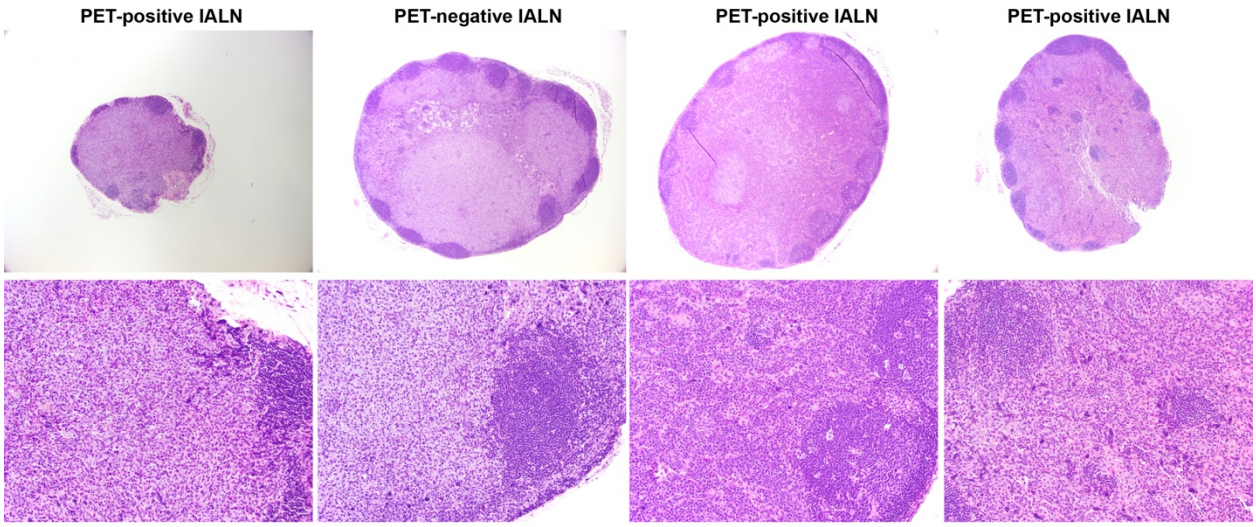

Figure S11. Morphologic (H&E) analysis of the vast majority of PET-positive ipsilateral axillary lymph nodes (IALNs) harvested from mice bearing subcutaneous OVCAR3 xenografts imaged with [^{89}Zr]Zr-DFO-muAR9.6 revealed no clear evidence of infiltrating neoplastic cells.

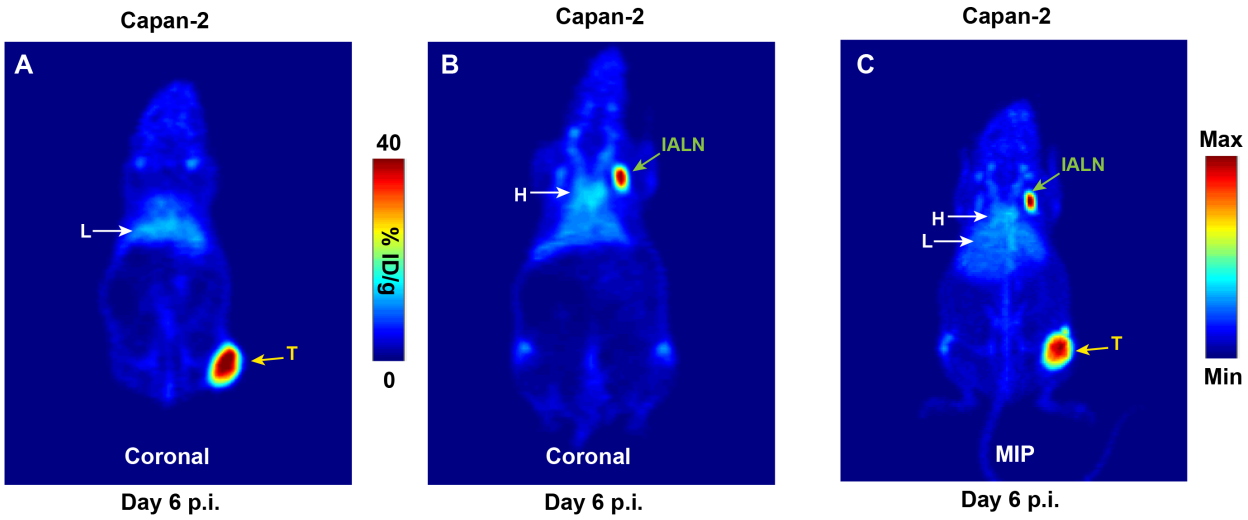

Figure S12. An isolated case of a mouse bearing a subcutaneous Capan-2 PDAC xenograft showing high uptake of [^{89}Zr]Zr-DFO-muAR9.6 via immuno-PET imaging. (**A-C**) PET images acquired 6 d after the administration of [^{89}Zr]Zr-DFO-muAR9.6 in a mouse bearing a subcutaneous Capan-2 xenograft; (**A**) Coronal slice revealing the high uptake of radioactivity in the tumor (T) on the lower right flank of the mouse; (**B**) Coronal slice highlighting the high radioactivity concentration in the ipsilateral axillary lymph node (IALN); (**C**) Maximum intensity projection (MIP) PET image of the same animal highlighting the relative radioactivity concentrations in the tumor and distant IALN. The maximum intensity projections have been scaled from 0-100%.

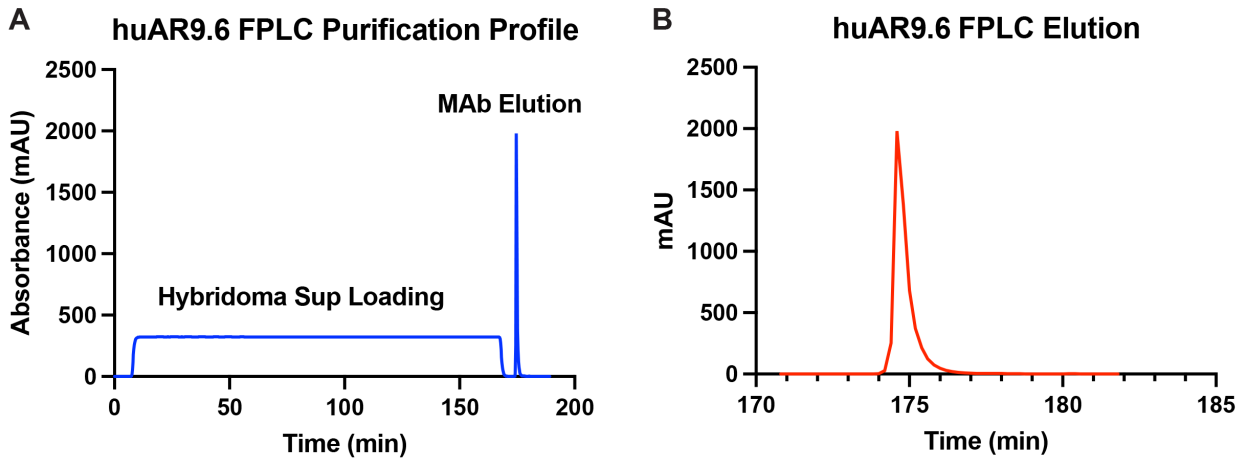

Figure S13. FPLC purification of recombinantly-expressed huAR9.6 antibody. (**A-B**) FPLC chromatogram showing protein G affinity chromatography-based single-step purification of the humanized mAb huAR9.6.

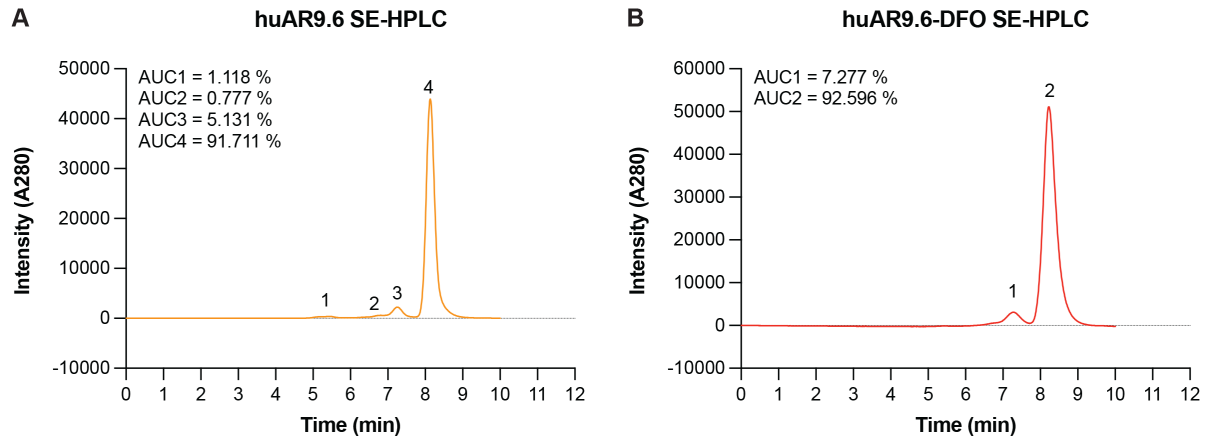

Figure S14. Size exclusion-high performance liquid chromatography (SE-HPLC) profiles of (A) huAR9.6 and (B) huAR9.6-DFO. SE-HPLC revealed ≥90% monomeric content (peak 4 in A) of muAR9.6 and its DFO-modified conjugate (peak 2 in B).

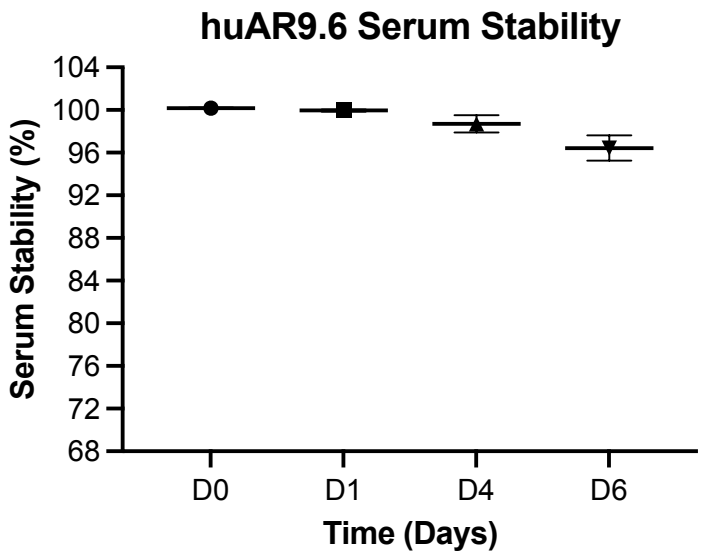

Figure S15. ***In vitro*** **serum stability of [^{89}Zr]Zr-DFO-muAR9.6.** [^{89}Zr]Zr-DFO-muAR9.6 demonstrated less than 5% demetallation in a biological medium (human AB type serum) up to 7 days suggesting high stability of the radioimmunoconjugate.

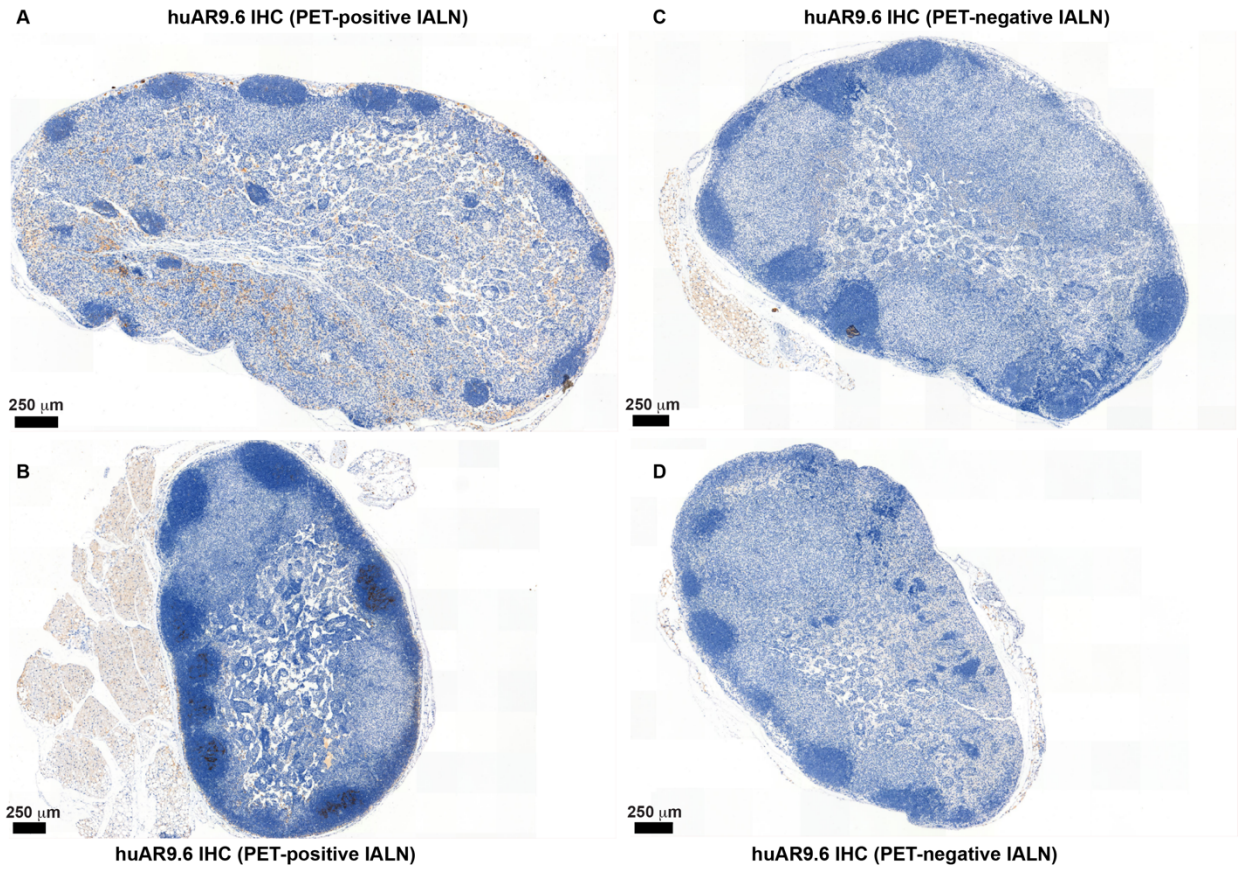

Figure S16. huAR9.6 IHC of PET-positive ipsilateral axillary lymph nodes (IALNs) show different staining pattern relative to PET-negative IALNs harvested from mice bearing OVCAR3 xenografts injected with [^{89}Zr]Zr-DFO-huAR9.6. (**A-B**) IHC-stained section of a PET-positive IALN showing huAR9.6 immunoreactivity (brown staining) in the subcapsular sinuses of the subcapsular space, cortex, and medullas. The PET-positive IALN in (**B**) also showed intense staining at the center of the lymphoid follicles, which was observed in multiple PET-positive IALNs (**C-D**) IHC-stained section of a PET-negative IALN showing the lack of huAR9.6 immunoreactivity (brown staining) in the same compartments outlined for the PET-positive counterparts. Note: images of the lymph nodes shown in *Figures S16A* and *S16B* are also shown in *Figures S17A* and *S17C*, respectively. In addition, an enlarged image of the lymph node shown in *Figure S16A* is shown in *Figure 6G* to highlight the cellular and acellular staining in the subcapsular sinus of this tissue.

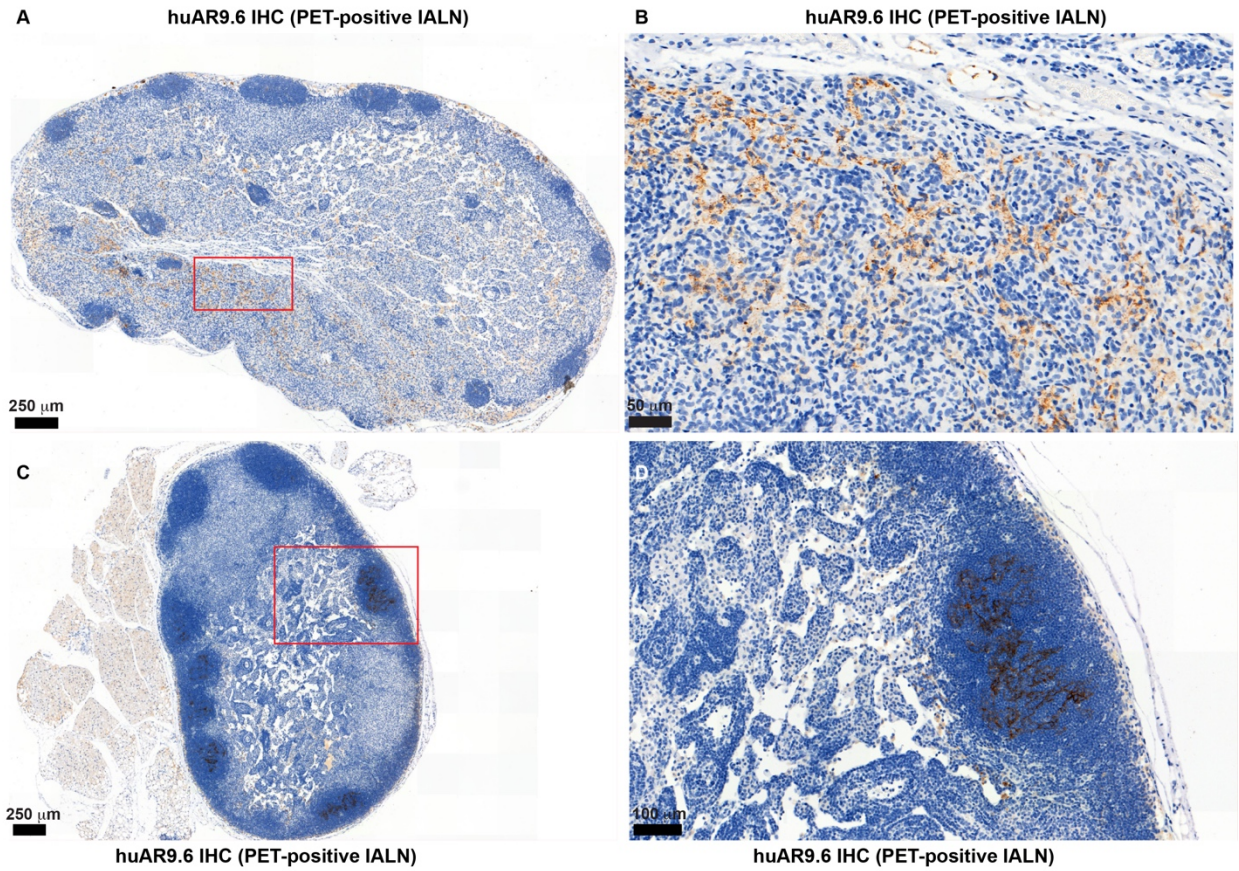

Figure S17. A closer look at the huAR9.6 IHC-positive and PET-positive ipsilateral axillary lymph nodes (IALNs) reveals amorphous staining in the cortical sinuses and strong cellular staining at the center of the lymphoid follicles. (**A**) IHC-stained section of a PET-positive IALN showing huAR9.6 immunoreactivity (brown staining) in the subcapsular sinuses, cortex, and medullas; (**B**) A magnified image of the boxed section outlined in (**A**) showing acellular/amorphous staining in the cortical sinuses suggestive of huAR9.6 immunoreactivity to shed antigen draining into the PET-positive IALN; (**C**) PET-positive IALN showing intense staining at the center of the lymphoid follicles; (**D**) A magnified image of the boxed section outlined in (**C**) showing intense staining in the lymphoid follicles that appears to be associated with an undetermined cell type. Note: images of the lymph nodes shown in *Figures S17A* and *S17C* are also shown in *Figures S16A* and *S16B*, respectively, to highlight other unique staining patterns observed within the lymphoid structures.